J Fail. Anal. and Preven. (2007) 7:464–474
DOI 10.1007/s11668-007-9083-8

P • E • E • R R • E • V • I • E • W • E • D

Numerical Simulation and Characterization of Slurry Erosion of Laser Cladded Surfaces by Using Failure Analysis Approach

Eswar Yarrapareddy · Radovan Kovacevic

Submitted: 21 May 2007 / in revised form: 8 October 2007 / Published online: 13 November 2007

Abstract A material failure model (MFM) of progressive damage initiation and propagation for the impingement of solid and liquid particles on the solid surfaces was used to numerically simulate the slurry erosion process. The commercially available 3D Finite Element Analysis (FEA) package ABAQUS/Explicit was used to evaluate this problem. The damage caused on the solid surfaces by the impingement of solid and liquid particles is called the slurry erosion. The proposed model uses the FEA concepts of adaptive meshing, strain-dependent damage initiation criteria, a general contact algorithm, damage propagation, enhanced hourglass section control, and multiple particle impingements to study the slurry erosion process. For the purpose of experimental validation and due to the availability of material properties, surface coatings of an alloy of steel are deposited by the Laser-Based Direct Metal Deposition (LBDMD) process. The slurry erosion tests are performed on these depositions using the ceramic proppant at different impingement angles. The tests are made in a centrifugal force driven erosion testing machine. From these tests, the material removal rate (MRR) values and depth of penetration including the profiles of the craters are computed as a function of the slurry jet impingement angles. The numerically computed results are compared with the experimental results and are shown to be in good agreement.

E. Yarrapareddy · R. Kovacevic (✉)
Center for Laser-Aided Manufacturing, Southern Methodist University, Dallas, TX 75205, USA
e-mail: kovacevi@engr.smu.edu

E. Yarrapareddy
e-mail: eyarrapa@smu.edu

Keywords Laser-based direct metal deposition · Finite element analysis · Adaptive meshing · Material failure analysis · Slurry erosion

Introduction

Materials systems developed for slurry erosion resistance can provide great benefits in many industries to improve the service life of systems and components that are exposed to a slurry erosion medium. Although these materials systems offer excellent resistance to erosion in general, they are potentially susceptible to damage when the slurry jet impacts the systems. Often, the damage in the erosion process resulting from impact is highly visible and exists in the form of crater profiles and material removal. However, the damage in the erosion process is affected by many process parameters such as the impingement jet velocity, angle of impingement, particle size and shape, and mechanical and microstructural properties of the target and the solid particles in the slurry [1]. It is difficult to monitor and study the influence of all these process parameters on the slurry erosion process by the experiments alone. Hence, the numerical simulation can provide the solution the need for extensive experimentation. Validated numerical simulation results, which could substitute for experiments, have potential applications in hydraulic turbines, slurry pumps, valves, pipelines conveying solid and liquid particles, and the marine, oil and gas production, and power generation industries.

Many researchers [2–7] have been working on the erosion process modeling using different modeling techniques and simulation mechanisms. In the early stages of the modeling of the erosion process, Finnie developed mathematical model mechanisms for ductile

metals [2] and solid surfaces [3] for a single particle impingement; Bitter developed erosion models [4–5] based on plastic deformation, cutting, Hertzian contact theory, and energy balance equation approaches; Hutchings [6] developed a theoretical model based on a plastic strain approach for metals by exposure to spherical particles at normal impingement; and Hashish [7] modified Finnie's models to include the effect of the particle shape.

In the last two decades, a number of researchers [8–15] have been working on the numerical modeling of the erosion process using different finite element analysis (FEA) packages. Woytowitz et al. [8] studied the erosion process from a solid mechanics perspective using nonlinear FEA. Chen et al. [9] presented a computational mean particle erosion model and had reasonable agreement with experimental results. Elalem et al. [10] developed a Micro-Scale Dynamic Model (MSDM) for simulating the wear behavior of materials on the microscales. Shimizu et al. [11] used Tabor's theory and Finite Element Method (FEM) for modeling the surface damage caused by the impact of solid particles in a gas or liquid stream. Chen et al. [12] used a MSDM for simulating the solid particle erosion process. Papini et al. [13] developed a computer algorithm model to account for the interference action between the rebounding and incident streams in erosion testing. Griffin et al. [14] developed a 3D FEA model for solid particle erosion using the element removal method. Eltobgy et al. [15] modeled the 3D erosion process and considered multiple particle interaction.

This article focuses on applying the failure analysis methodology to simulate the erosion process using commercially available ABAQUS/Explicit analysis software. The damage initiation and propagation of the solid surfaces is modeled for multiple particles. The numerical simulation results of solid surfaces are validated with an experiment, and the experimental results are in reasonable agreement with the simulations.

Experimental Process Details

Details of Materials

The metallic premixed A11–LVC steel powders are used for the development of surface coatings by Laser-Based Direct Metal Deposition (LBDMD). The chemical composition of this powder is shown in Table 1. The mesh size and apparent density of this powder is −80 + 270 mesh and 4.2 g/cc, respectively. The morphology of the powder is shown in Fig. 1a. This powder mixture consists of spheroidal and nodular particles. The absence of flake-shaped particles can partially explain why this powder works well for laser direct metal deposition process applications. The processes of laser cladding and laser deposition generally work well with spheroidal particles, while success with flakey particles is far more limited due to the high surface area-to-volume ratio of flake-shaped particles. Thin flat particles tend to super heat when exposed to the laser heat source, resulting in poor depositions. An AISI 4140 steel plate with approximate dimensions of 30.4 mm × 25.4 mm × 6.4 mm is used as a substrate for all depositions. The chemical composition of AISI 4140 steel is 0.38–0.43 C, 0.75–1.00 Mn, 0.15–0.35 Mo, 0.8–1.10 Cr, max 0.035 P, max 0.04 Si, and the balance is Fe. A semi-crystalline alumina silicate proppant called Econoprop 20/40 of mesh size −20 + 30 is used as a ceramic proppant for slurry erosion testing. The nominal chemical composition of this proppant is shown in Table 2, and its morphology is shown in Fig. 1b. The Econoprop consists of spheroidal mineral particles with a uniform shape and a narrow size distribution.

Table 1 The chemical composition of A11-LVC

Element	C	Si	Mn	P	S	Cr	Ni	Mo	V	N	Fe
Weight %	1.82	0.86	0.49	0.017	0.010	5.45	0.07	1.39	9.04	0.117	bal

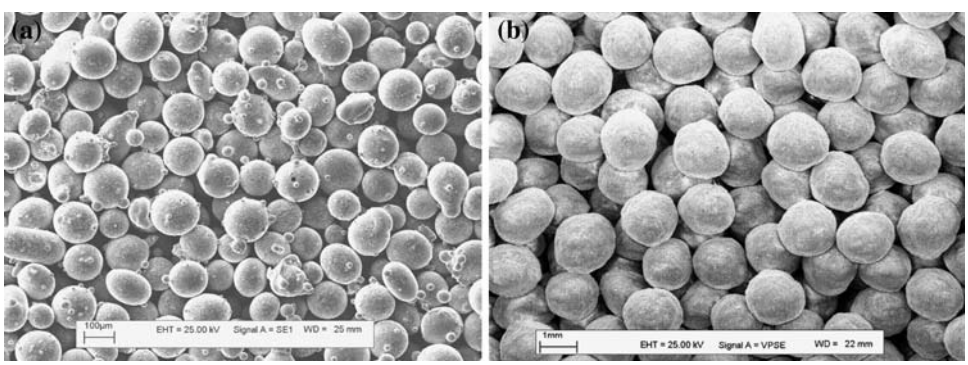

Fig. 1 The morphology of (**a**) the A11-LVC alloy powder used for deposition and (**b**) the Econoprop 20/40 used for erosion testing. Note the difference in magnification between the micrographs

Table 2 The chemical composition of Econoprop 20/40

Ingredients	Percentage concentration
Silicon dioxide amorphous	5–35
Mullite crystalline	60–85
Silica crystalline	0–20

MultiFab System at SMU

The Center for Laser Aided Manufacturing at Southern Methodist University has been developing a multifunctional hybrid fabrication system for rapid manufacturing (RM) and repair called Multi Fabrication (MultiFab) [16]. The MultiFab is based on additive and subtractive procedures and is able to build the materials directly from the metal/ceramics powders using the laser or microplasma as a heat source.

The MultiFab system consists of a 5-axis vertical CNC machining center for positioning, milling, drilling, and taping operations, with a 16-tool tool exchanger, a 6-axis robot to manipulate and control the microplasma welding torch, a multimode laser beam for laser metal deposition. The laser beam is generated by a Nd: YAG laser of 1 kW in power, operated in a continuous wave (cw) mode and in a modulated mode at 2.5 kW. The laser beam is delivered to the laser head through a 1,000-μm step-index fiber optic cable. The laser head is mounted on the 6-axis robot, and is cooled by water. The laser head is equipped with four radially symmetric nozzles set at 30 degrees with respect to the vertical axis. These nozzles deliver powder carried by an inert gas (Argon) to the laser focal point (or molten pool). Two servo-motor driven powder feeders provide a stable powder flow for powder delivery. The control system of the laser deposition process is based on a high-frame rate CCD camera equipped with an infrared (IR) filter to capture the shape of the molten pool in real time [17], and a laser diode is used for the buildup height measurement. Both the camera and diode laser are installed on the laser head. The CCD camera is coaxial with respect to the laser beam. The MultiFab system is shown in Fig. 2. The MultiFab system can be used for the LBDMD process as well as for the Micro-Plasma Deposition (MSD) process.

A11- LVC Steel Deposition Profiles and Process Parameters

The A11-LVC steel powders are deposited on 4140 steel substrate plates. Two layers of A11-LVC steel powder compositions are deposited on the substrate to build the surface coating to an approximate size of 30 mm × 30 mm × 1.72 mm. The deposition profile used for surface coatings is shown in Fig. 3. These coatings are fabricated with a laser beam power of 350–380 Watts and a 1-mm diameter laser spot. Higher laser power is used for the first layer, and lower values are used for the second layer. The linear traverse speeds are variable but in the range 8–10 mm/sec, and powder delivery speeds are also available but in the range 8–10 g/min with argon as a powder carrier. Each layer is 0.43-mm high and 1-mm wide. A 40% overlap of successive melting layers is used to provide a uniform surface of the coating.

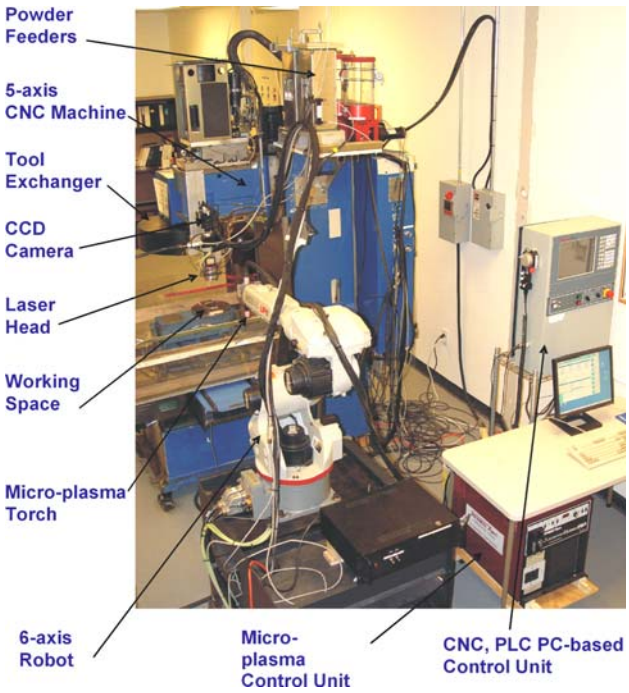

Fig. 2 The MultiFab System developed at the Center for Laser-aided Manufacturing of SMU

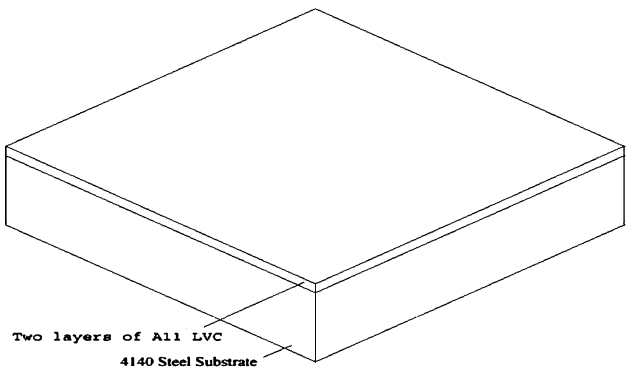

Fig. 3 The schematic representation of deposition profile used for building the coating of A11-LVC

The Slurry Erosion Machine, Samples Testing Conditions and Parameters

The slurry erosion tests are conducted at room temperature using the slurry erosion testing machine shown in Fig. 4a. The machine consists of two tanks, vertically arranged, with a motor-driven axle running through the upper tank and down into the lower tank. The rotation of the axle provides a centrifugal force that drives the circulation of fluid through the test machine. The upper tank encloses a pair of jet orifice assemblies attached at the ends of the two hollow arms, which hold the test samples at a fixed position relative to the slurry jet. The orifices are each 6.4-mm wide. Fluid that flows out of the orifices during testing first strikes the samples as shown in Fig. 4b, then falls to the bottom of the upper tank where it is funneled through a single large orifice to fall to the lower tank. The lower tank serves as a slurry reservoir for the test machine. A mixing propeller at the bottom of the axle stirs the slurry in the lower tank and provides a near-homogenous mixture of water and alumina silicate called Econoprop 20/40.

For all experiments, the slurry concentration is 22.73 kilograms (50 pounds) of Econoprop 20/40 in 94.64 liters (25 gallons) of water. This concentration is maintained constant in all tests. Experiments are carried out at a slurry impingement velocity of 25 m/sec and at 30-, 45-, and 90-degree impingement angles. The impingement time used is 10 min per test sample. The mixing propeller speed is set at 875 rpm for all experiments. The test samples are cleaned with methyl alcohol before and after testing, and weighed for the mass loss using an electronic scale with an accuracy of 0.1 mg. Two samples are used for each impingement angle and, hence, six samples are tested altogether. The mass loss per unit amount of time is called the material removal rate (MRR) and is calculated using the following formula.

$$\text{Material Removal Rate (MRR)} = (W_i - W_f)/(\text{Unit Amount of Time}) \quad (1)$$

where W_i is the initial mass of each sample, and W_f is the final mass after erosion testing.

Test Samples Preparation and Characterization

The as-deposited surface coatings are surface ground to remove the loose, unmelted powder particles and to remove protruding corner depositions from the surfaces of the deposits. The samples are surface ground until a smooth surface appears. This grinding is necessary in order to achieve accurate MRR values. Scanning Electron Microscopy (SEM) is used to observe the surfaces and subsurfaces of the eroded samples to evaluate the damage initiation and the successive damage propagation. The damaged samples surfaces are also characterized by measuring the maximum penetration depth of the crater formed by the slurry jet using the needle-shaped probe and a linear scale with a digital readout.

Finite Element Model Based on Damage Initiation and Propagation

Finite Element Model Formulation

The objective of the erosion process modeling is to determine the damage initiated by the impact of solid particles. The impact effect of the liquid particles is neglected due to the unavailability of these kinds of elements in ABAQUS. However, a recommended procedure given in section "Conclusions and Future Recommendations" would give the exact solution of the erosion process. So, during this process, a large deformation occurs on the target sample. Hence, this process is simulated using the commercially available three-dimensional FEA ABAQUS/Explicit software with the material failure model (MFM) approach. ABAQUS/Explicit offers a general capability for modeling

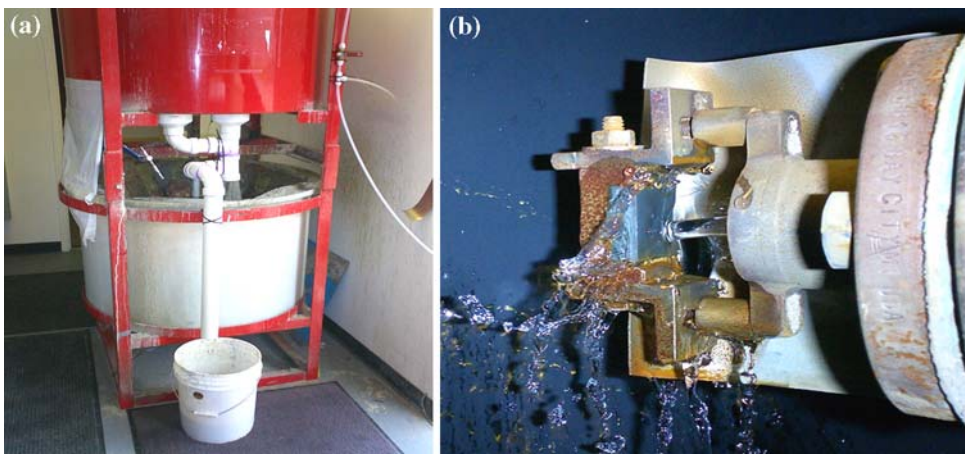

Fig. 4 The slurry erosion testing set up (**a**) showing the upper and lower tanks and (**b**) the slurry jet impinging the test sample at 90° angle

the damage initiation and propagation during the erosion process. The erosion process is modeled with the general contact algorithm using the element-based surfaces with adaptive meshing for the large deformation of the damaged target elements. A general contact algorithm between the multiple solid particles and the target used by the ABAQUS/Explicit solver is a computationally efficient way of solving the erosion process when compared with an implicit solver.

Governing Equations for Damage Initiation

The damage initiation criterion is a phenomenological way of predicting the onset of damage due to the impact of solid particles onto the target surface. This finite model assumes that the equivalent plastic strains at the onset of damage, $\varepsilon_{\mathrm{D}}^{-pl}$, is a function of stress triaxiality and the strain rate [18]:

$$\varepsilon_{\mathrm{D}}^{-pl}(\eta, \dot{\varepsilon}^{-pl}) \tag{2}$$

where $\eta = -p/q$ is the stress triaxiality, p is the pressure stress, q is the Mises equivalent stress, and $\dot{\varepsilon}^{-pl}$ is the equivalent plain strain rate. The criterion for damage initiation is met when the following condition is satisfied.

$$\omega_{\mathrm{D}} = \int \frac{d\varepsilon^{-pl}}{\varepsilon_{\mathrm{D}}^{-pl}(\eta, \dot{\varepsilon}^{-pl})} = 1 \tag{3}$$

where ω_{D} is a variable that increases monotonically with the plastic deformation of the target surface. At each increment during the erosion process, analysis of the incremental increase in ω_{D} is computed by

$$\Delta\omega_{\mathrm{D}} = \int \frac{d\varepsilon^{-pl}}{\varepsilon_{\mathrm{D}}^{-pl}(\eta, \dot{\varepsilon}^{-pl})} \geq 0 \tag{4}$$

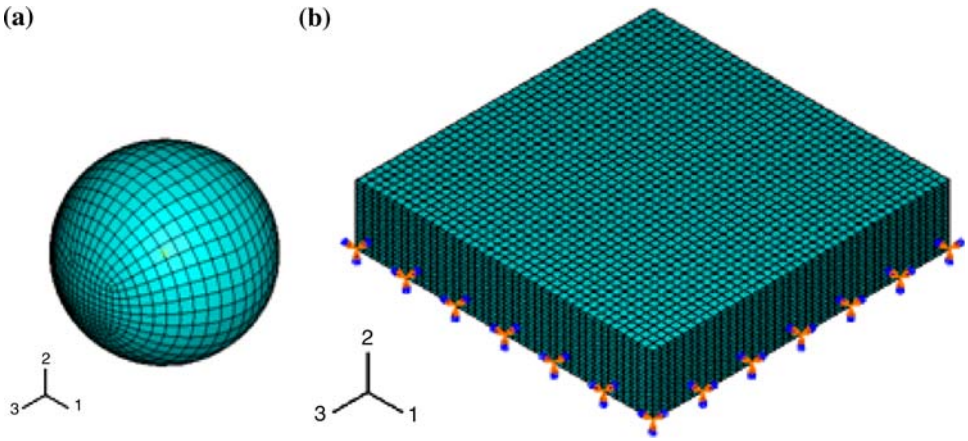

Fig. 5 The schematic representation of (**a**) one of the solid particles used for impingement and (**b**) the target surface meshing and boundary conditions. The solid body particle is magnified to some extent to give the better view

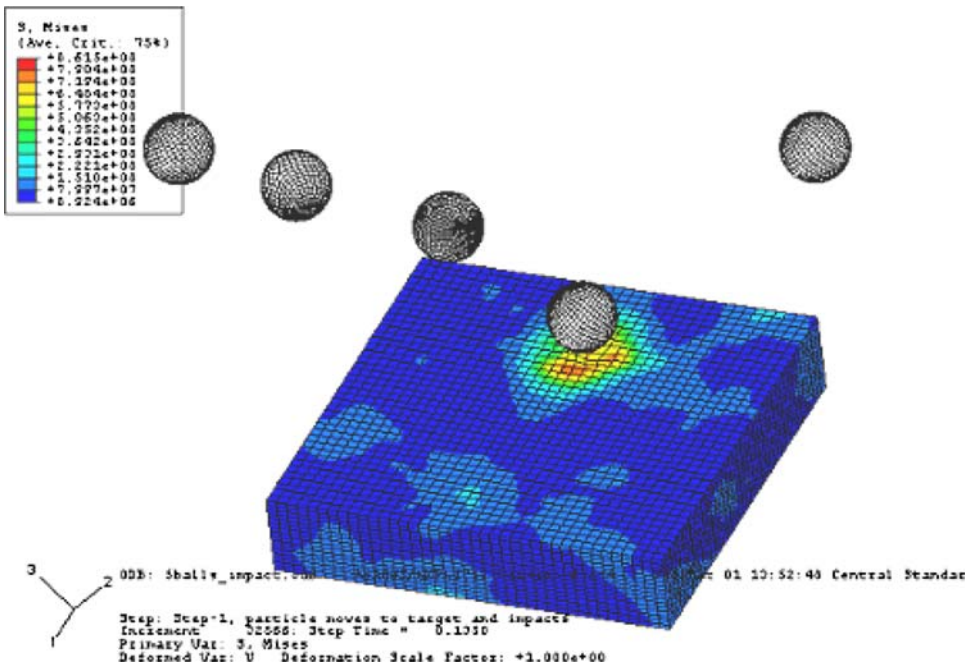

Fig. 6 The proof of concept that the erosion caused by the damage of the first particle impingement on the surface coating

General Contact Algorithm and Adaptive Meshing

ABAQUS/Explicit provides the general (automatic) contact algorithm between the solid particles and the deformable target surfaces. The general contact algorithm allows the element-based surfaces to be defined on the eroding bodies; hence, the contact can be defined between any number of solid bodies and the eroding surfaces. The contact pair algorithm, which is another kind of contact interaction available in ABAQUS/Explicit, has more restrictions for the element-based surfaces in the erosion process. A node-based surface must be used to model the eroding target surface if the contact pair algorithm is used. The solid body particles are set as master surfaces, and the target surfaces are set as slave surfaces. The Coulomb friction between the target contact surface and the solid particles is defined using the equation below.

$$F_{\mathrm{f}} = \mu N \tag{5}$$

where μ is the coefficient friction, N is the force normal to the contact target surface, and F_f is the force exerted by the friction. This force is exerted in the direction opposite to the motion of solid particles. The coefficient friction (μ) between the target surface and the solid particles is assumed as 0.4, which is reasonable for the dissimilar materials used in this study.

Adaptive meshing in ABAQUS/Explicit allows the mesh to move independently of the deformed or damaged target

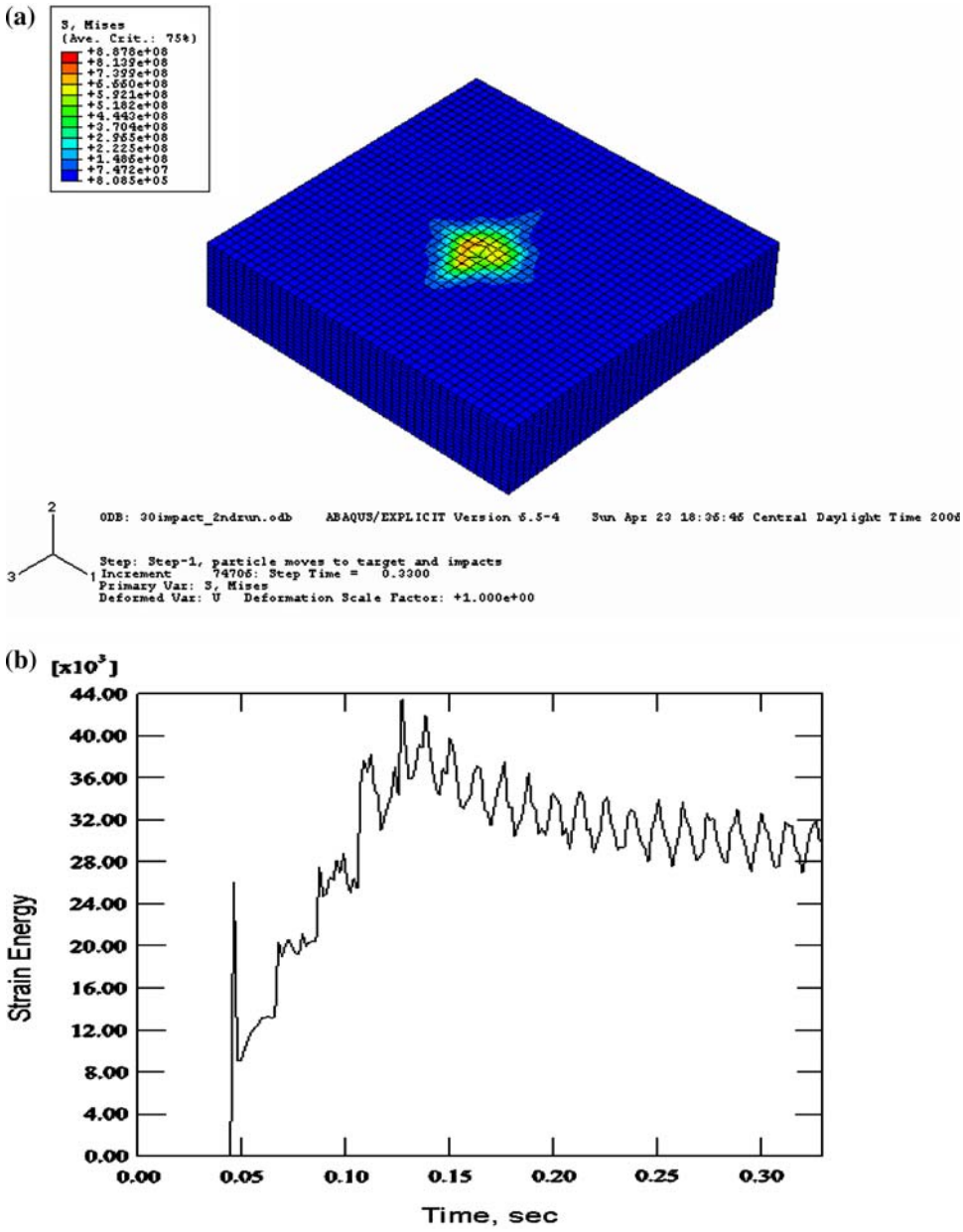

Fig. 7 The numerical simulation results for 30° impingement angle showing (**a**) the accumulated damage area on the surface coating and (**b**) the relationship between the change of strain energy with respect to the time

material. Adaptive meshing does not alter the topology of the elements and connectivity of the mesh when there is a large deformation or damage in the material [18]. This adaptive meshing technique in ABAQUS combines the features of pure Lagrangian analysis and pure Eulerian analysis. Hence, this type of adaptive meshing is often referred to as Arbitrary Lagrangian–Eulerian (ALE) analysis.

Meshing Elements and Boundary Conditions

The target surface coatings are modeled as deformable rigid bodies with C3D8R meshing elements, which are 8-node linear brick elements, and the impingement solid particles are modeled as discrete rigid bodies with R3D4 meshing elements, which are 4-node 3D bilinear rigid quadrilateral elements. The schematic representation of the solid particles and the target surfaces is shown in Fig. 5. The target surface is of dimensions 30 mm × 30 mm × 6 mm approximately, and the solid particle is 1-mm wide. The deposited surface coatings and substrate are considered together for modeling as shown in Fig. 5 b.

The target work surface constrained the displacement and rotation at the bottom of it in the X (1), Y (2), and Z (3) directions. The representation of these constraints is shown in Fig. 5b. For the solid particles, an initial velocity

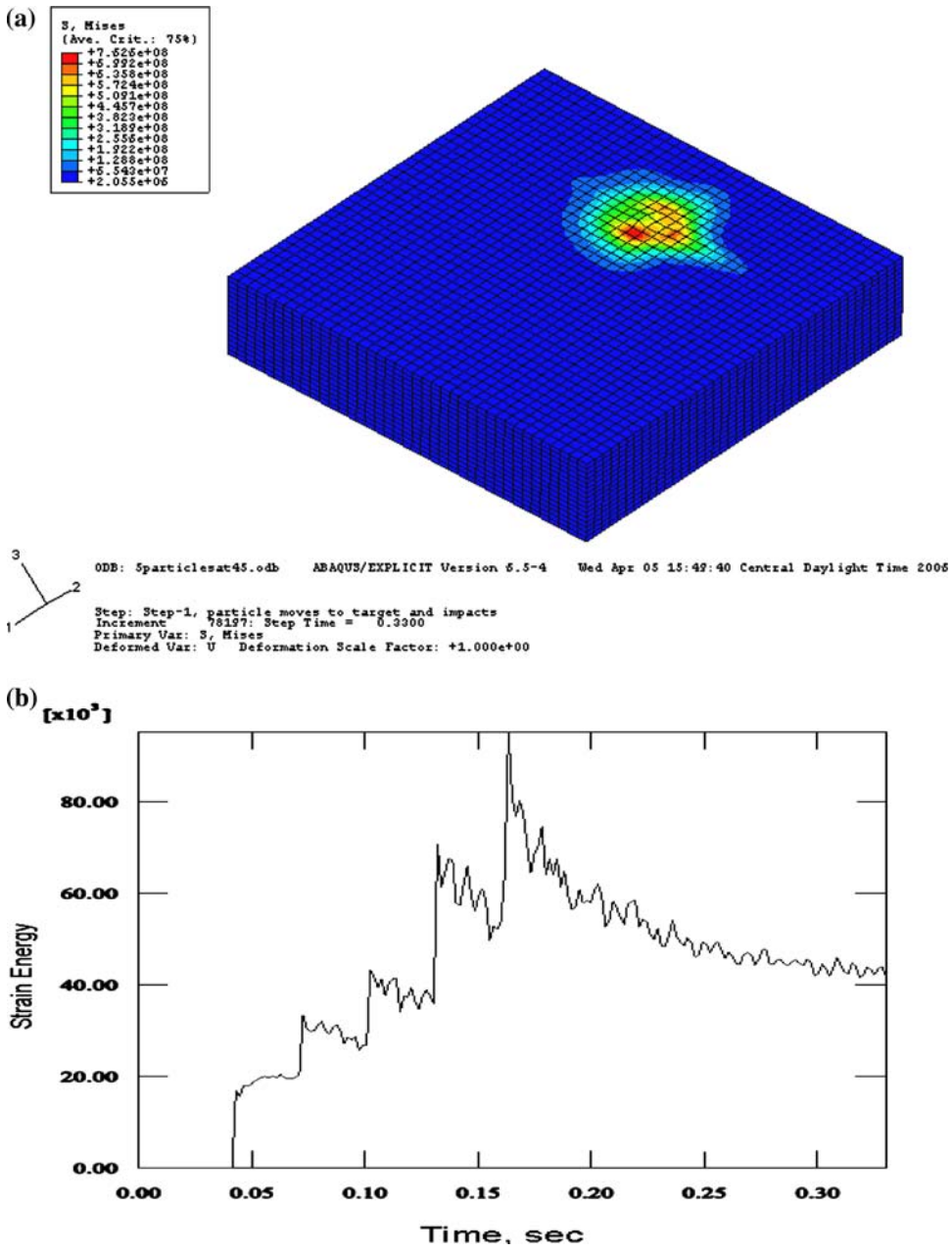

Fig. 8 The numerical simulation results for 45° impingement angle showing (**a**) the accumulated damage area on the surface coating and (**b**) the relationship between the change of strain energy with respect to the time

distribution of 25 m/sec is assumed because this velocity is used in the experimental part. The contact among the particles is not defined, and they are placed 2 mm apart.

Numerical Simulation Results and Discussions

Simulation Results for Surface Coatings

The initial simulations are carried out by five solid particles impinging the target surface at a 45-degree impingement angle. From this simulation, it is concluded that the erosion would occur on the surface of the coating by the damage initiation caused by the solid particles impingement. This damage was propagated for successive impingement of the particles. The proof of concept for the erosion crater profile formed after the impingement of the first particle is shown in Fig. 6.

In light of the above simulation results, a thorough assessment and more simulations are carried out at the different impingement angles of 30, 45, and 90 degrees. These simulation results show that the elements within the contact domain failed based on the material damage/failure mechanism. The general contact considers the exposed faces only for the element failure, and the underlying elements have not failed. Thus, the exterior faces of the

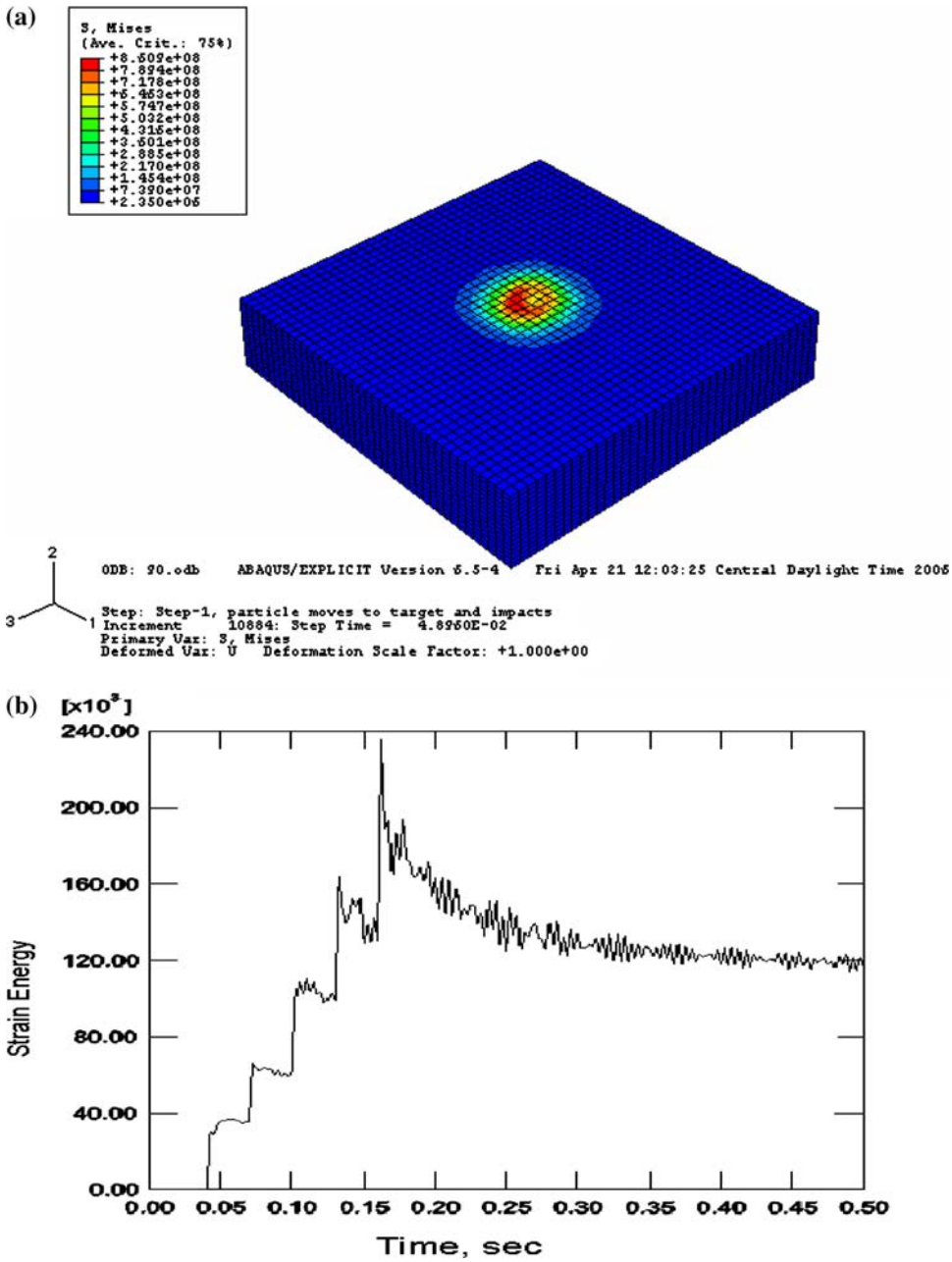

Fig. 9 The numerical simulation results for the 90° impingement angle showing (**a**) the accumulated damage area on the surface coating and (**b**) the relationship between the change of strain energy with respect to the time

elements are initially active, and the interior faces are initially inactive. Once the exterior element fails, then its faces are removed from the contact domain, and the exposed underlying exterior faces become active. This process is progressive for successive impingements. Hence, the general contact between the impinging particles and the target surface coating supports the idea of a damage/failure mechanism [18].

For a 90-degree impingement angle, the area of the crater, i.e., the damaged area formed is higher than the areas of the craters formed at 45- and 30-degree impingement angles. These differences in the areas of the craters formed are inevitable and attributed to the angle of impingement and the longer contact time of the solid particles on the surface coating. Figure 7a shows the accumulated damage that occurred from the 30-degree impingement angle of the solid particles, and Fig. 7b shows the accumulated strain energy over a period of time for five impinged particles. Figure 8a shows the accumulated damage by the stream of five particles at a 45-degree impingement angle, and Fig. 8b shows the change of strain energy with respect to time. Figure 9a illustrates the damage accumulated by the normal impingement of the particles, and Fig. 9b presents the changed strain energy with respect to time, and the increment in the strain energy for each and every impingement of the particles.

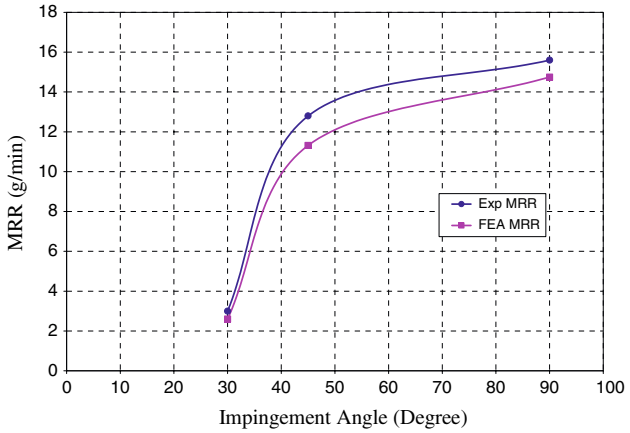

Fig. 10 The MRR values obtained from FEA simulation and the experimental results

Material Removal Rates and Depth of Penetrations

The MRRs in numerical simulations are calculated from the mass and density of the deposited surface coating and the substrate used. The initial mass of the deposited surface coating is 36.45 grams including the substrate used. For the surface coating, the finite element model contains a total number of 27,835 elements. Hence, the mass of each finite element is 1.309×10^{-3} grams. The MRR values are calculated by multiplying the mass of each finite element and the number of failed finite elements over the time of each impingement. These MRR values are compared with the experimentally found MRR values for the ten minutes time used in the experiments, as shown in Fig. 10. The FEA calculated MRR values are in good agreement with the experimental values.

The maximum depths of penetrations are calculated based on the distance from the damaged element to the undamaged element in the impingement area. The longitudinal cut of the damaged area, which is used for calculating the depth of penetrations, is shown in Fig. 11. The FEA-measured depths of penetration are shown in Fig. 12, and they are in good agreement with the experimental results.

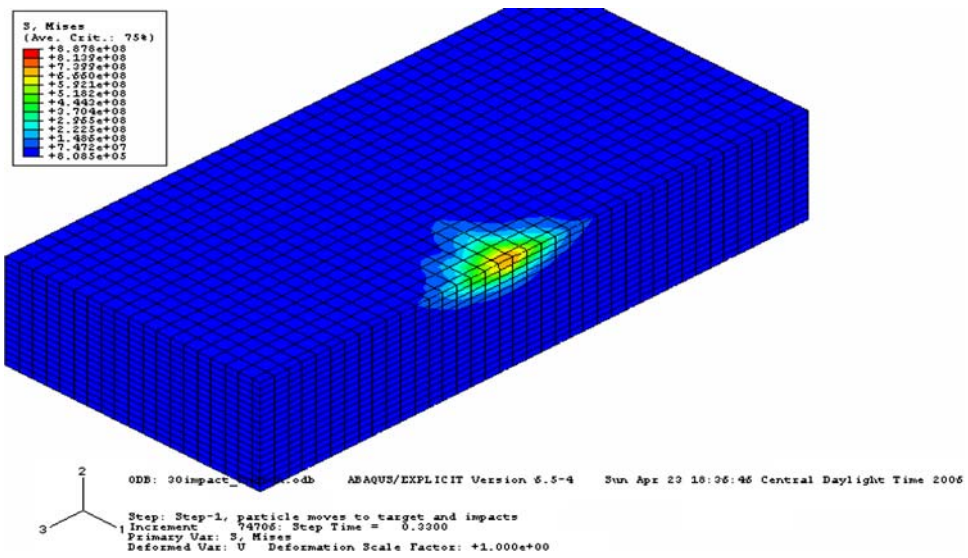

Fig. 11 One of the longitudinal views of the damaged surface coatings that is used for calculating the depth of penetrations

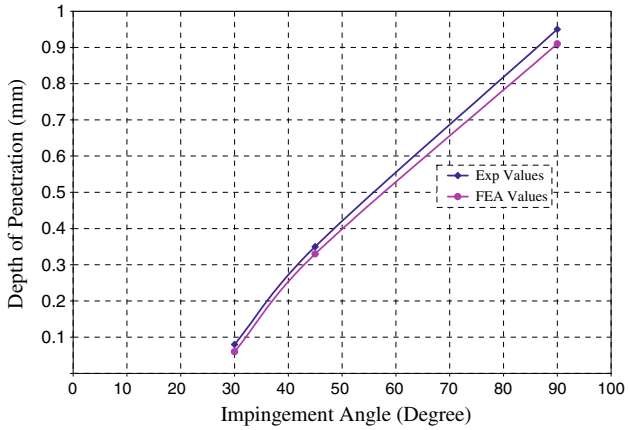

Fig. 12 The depth of penetration values obtained from FEA simulation and the experimental results

SEM Characterization of Slurry Eroded Surfaces

The slurry eroded surfaces of the A11-LVC steel are characterized by SEM in order to understand the characteristic features of erosion surfaces, sub-surfaces, and the erosion mechanism. Figure 13 shows the typical SEM images of A11-LVC steel damaged surfaces at different impingement angles. These surface coatings are damaged, and the material removed by the high velocity slurry jet containing both the solid and liquid particles at different impingement angles. The damage to the material occurs when the equivalent plastic strain of the material exceeds its failure criteria values. This damage is propagated for successive impingements causing microcutting and material removal from the surface of the material. Figure 13a illustrates the damage from a 90-degree impingement angle, and shows the severely damaged surfaces, sub-surfaces, and high depth of field. An increasing number of pits and a high degree of microcutting of the material are present. Figure 13c shows a lower number of pits and fewer microcracks on the surface of the sample impinged by a 30-degree slurry jet. Finally, the depth of field employed while viewing the samples in the SEM is directly proportional to the jet impingement angle used for a given sample, which supports the earlier penetration depth measurements from the ABAQUS/Explicit analysis and experimental results indicating that larger jet angles create deeper erosion crater zones in the samples.

Conclusions and Future Recommendations

A MFM methodology was used to simulate the 3D erosion process by using the commercially available FEA software, ABAQUS/Explicit. This model used the FEA concepts of ALE formulation, adaptive meshing, multiple particle impingement, and material failure. This model provides the prediction of the areas of the craters formed during the erosion process, and the amount of material deformed on the surface coating. These numerical simulation results were compared with the experimental results and are in coincidence. Also, the results obtained demonstrate that the

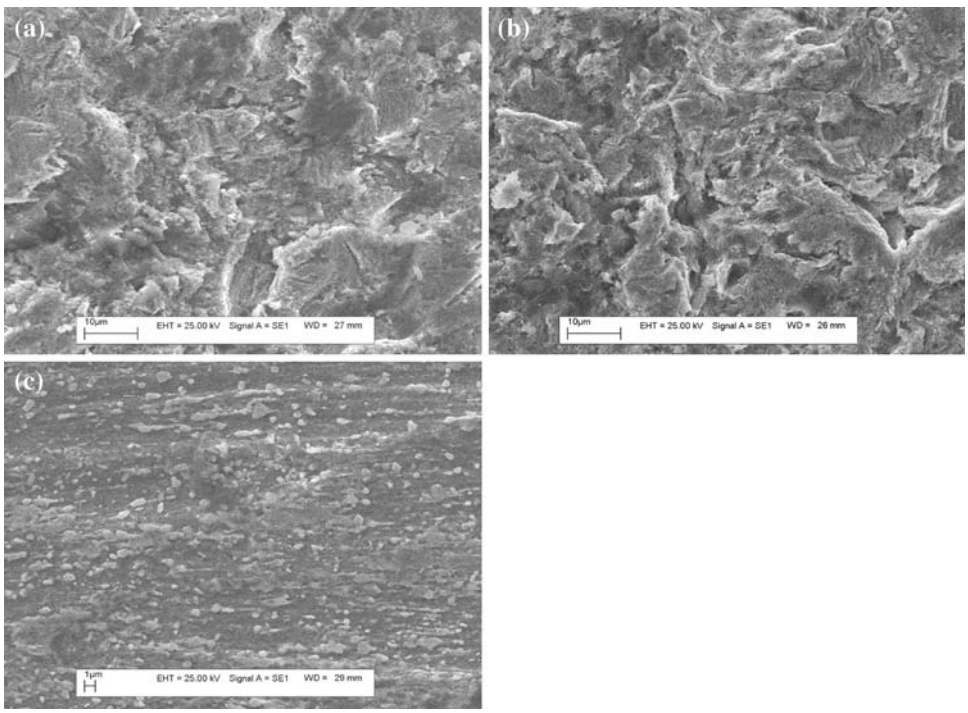

Fig. 13 Typical SEM microstructures of slurry eroded A11-LVC steel samples tested at (**a**) 90° (**b**) 45° and (**c**) 30° impingement angles. Note the difference in magnification among the micrographs due to difference in depth of the craters

predicted erosion location was also susceptible to the numerical simulation procedure implemented.

The numerical simulation results, which substitute the need for exercising experimentations, have potential applications in hydraulic turbines, slurry pumps, valves, and pipelines conveying solid and liquid particles, and the marine, oil and gas production, and power generation industries.

At higher impingement angles, the materials were severely eroded due to damage initiation causing a higher degree of microcutting and material removal. This damage was propagated for successive impingements.

The authors recommend that future research efforts focus on the implementation of the complete Fluid-Structure-Interaction (FSI) simulation for the cases of solid and liquid particle impingement on the target surface coatings. As the interaction between the fluid flow fields and the structural fields is expected to be quite large, it is impractical to attempt a solution by iterating between a Computational Fluid Dynamics (CFD) analysis and FEM analysis. Instead, a cosimulation approach should be used, in which the two analyses are used together. This approach requires a link between the two software packages, so that information such as pressure, temperature, solid boundary location, and so on can be transferred between the two analysis tools as they step forward in time. Fraunhofer SCAI has created an interface coupling between ABAQUS and FLUENT that is based on industry-standard scalable interprocess communication and mapping tools, called Mesh-based Parallel Code Coupling Interface (MpCCI) [19]. Hence, the authors recommend focus on the implementation of MpCCI for FSI simulation for the case of slurry erosion.

Acknowledgments The authors would like to acknowledge the financial support from Halliburton Energy Services through joining the NSF Industry University Co-operative Research Center for Laser Aided Manufacturing program. The authors would like to acknowledge Mr. Suresh Krishnan of ABAQUS South for his help with the numerical simulation; Mr. Michael Valant, Dr. Srdja Zekovic, and Dr. Vijay Soundararajan of SMU RCAM/CLAM for their help in performing the experiments and numerical simulation; Dr. Syed Hamid and Dr. Haoyue Zhang of Halliburton Energy Services for technical discussions; and Mr. Roy Beavers of SMU for SEM support. The A11-LVC steel alloy powders and Econoprop 20/40 are supplied by Carpenter Powder Products and Carbo Ceramics, respectively.

References

1. Hutchings I.M., Hutchings I.: Tribology: Friction and Wear of Engineering Materials. 2nd edn. Butterworth-Heinemann Press, London (1992)
2. I. Finnie: The mechanism of erosion of ductile metals. Proceedings of the Third National Congress on Applied Mechanics, New York, 1958, pp. 527–532
3. Finnie, I.: Erosion of surfaces by solid particles. Wear **3**, 87–103 (1960)
4. Bitter, J.: A study of erosion phenomena, part 1. Wear **6**, 5–21 (1963)
5. Bitter, J.: A study of erosion phenomena, part 2. Wear **8**, 161–190 (1963)
6. Hutchings, I.M.: A model for the erosion of metals by spherical particles at normal incidence. Wear **70**, 269–281 (1981)
7. Hashish, M.: An improved model of erosion by solid particle impact. 7th International Conference on Erosion by Liquid and Solid Impact, Cambridge, pp. 461–480 (1987)
8. Woytowitz, P.J., Richman, R.H.: Solid mechanics modeling of erosion damage. In: McDowell, D.L. (ed.) Applications of Continuum Damage Mechanics to Fatigue and Fracture, ASTM STP 1315, American Society for Testing and Materials, pp. 186–199 (1997)
9. Chen, D., Sarumi, M., Al-Hassani, S.T.S.: Computational mean particle erosion model. Wear **214**, 64–73 (1998)
10. Elalem K., Li D.Y.: Dynamical simulation of an abrasive wear process. J. Comput. Aid. Mat. Des. **6**, 185–193 (1999)
11. Shimizu, K., Noguchi, T., Seitoh, H.¸Okada, M., Matsubara, Y.: FEM analysis of erosive wear. Wear **250**, 779–784 (2001)
12. Chen, Q., Li, D.Y.: Computer simulation of solid particle erosion. Wear **254**, 203–210 (2003)
13. Papini, M., Ciampini, D., Krajac, T., Spelt, J.K.: Computer modeling of interference effects in erosion testing: effect of plume shape. Wear **255**, 85–97 (2003)
14. Griffin, D., Daadbin, A., Datta, S.: The development of a three-dimensional finite element model for solid particle erosion on an alumina scale/MA956 substrate. Wear **256**, 900–906 (2004)
15. Eltobgy, M.S., Ng, E., Elbestawi, M.A.: Finite element modeling of erosive wear. Int. J. Mach. Tool. Manu. **45**, 1337–1346 (2005)
16. Kovacevic, R.: System and method for fabrication and repairing part. US Patent 7,020,539, 28 March 2006
17. Kovacevic, R., Hu, D., Valant, M.: System and method for controlling the size of the molten pool in laser-based additive manufacturing. US Patent 6,995,334, 7 February 2006
18. ABAQUS Inc., Volume II—Analysis User's Manual, V.6.5, (2005)
19. http://www.abaqus.com/solutions/tb_pdf/TB-05-FSI-2.pdf